Journal of Applied Physics

RESEARCH ARTICLE | DECEMBER 09 2025

Fabrication and characterization of 115 GHz double split ring resonator

Gem Nakamura ; Yuhang Ren ; Michael Coumans; Laura Mugica; Sola M. Takahashi ; Anton Savitsky ; Dieter Suter ; Susumu Takahashi

J. Appl. Phys. 138, 223105 (2025)
https://doi.org/10.1063/5.0300520

Journal of Applied Physics ARTICLE pubs.aip.org/aip/jap

Fabrication and characterization of 115 GHz double split ring resonator

Cite as: J. Appl. Phys. 138, 223105 (2025); doi: 10.1063/5.0300520
Submitted: 2 September 2025 · Accepted: 19 November 2025 ·
Published Online: 9 December 2025

View Online Export Citation CrossMark

Gem Nakamura,[1] Yuhang Ren,[1] Michael Coumans,[2] Laura Mugica,[2] Sola M. Takahashi,[2] Anton Savitsky,[3] Dieter Suter,[3] and Susumu Takahashi[1,2,a)]

AFFILIATIONS

[1]Department of Physics and Astronomy, University of Southern California, Los Angeles, California 90089, USA
[2]Department of Chemistry, University of Southern California, Los Angeles, California 90089, USA
[3]Fakultät Physik, Technische Universität Dortmund, Dortmund D-44221, Germany

[a)]**Author to whom correspondence should be addressed:** susumuta@usc.edu

ABSTRACT

Electron paramagnetic resonance (EPR) spectroscopy requires an efficient coupling of electromagnetic waves over a sample volume. However, it is often challenging when EPR is operated in the terahertz (THz) range. Here, we report the fabrication and characterization of double split-ring resonators (DSRRs) designed to operate at a frequency of 115 GHz. The DSRR device consists of the outer and inner rings with diameters of 190 and 50 μm, respectively. Both rings have gaps, located on opposite sides, to concentrate and enhance the induced magnetic fields within the rings. The DSRR devices are fabricated using a wet-etch photolithography process. We also develop a characterization method to measure the resonant frequencies and Q-factors of individual DSRR devices. The developed DSRR fabrication method is useful for the development of resonators for various THz experiments.

I. INTRODUCTION

The terahertz (THz) range of the electromagnetic spectrum lies between microwaves and far-infrared waves. It is often considered as electromagnetic radiation from a frequency range of 0.1–10 THz. THz radiation has many unique characteristics and has been found to be very useful in science and technology.[1] For example, because the photon energies of the THz radiation coincide with molecular vibrations and rotations, THz spectroscopy is used for molecular vibrational and rotational spectroscopy.[2–4] THz radiation is promising for non-ionizing and non-invasive imaging because of its ability to penetrate a variety of materials.[5–8] In addition, THz radiation is useful for electron paramagnetic resonance (EPR) and related techniques because EPR spectroscopy can gain high spectral resolution and high sensitivity by operating with THz radiation.[9–15] The high spin polarization achieved from the high-frequency EPR also has a significant advantage in studying spin decoherence mechanisms in various spin systems.[12,16–19]

In THz spectroscopy and EPR spectroscopy, a high intensity of THz waves at the sample is crucial for enhancing the signal-to-noise ratio in the measurement. The employment of a resonator is a common method to increase the intensity of electromagnetic waves at the sample without increasing the incident power. For EPR spectroscopy and related techniques, various types of resonators have been developed.[20] In a range of microwave frequencies, a rectangular and a cylindrical cavity are commonly used.[20,21] However, in a range of THz frequencies, because the detection volume of a cavity resonator is proportional to the cubic power of the wavelength, the employment of the cavity resonator accompanies a smaller sample volume. The smaller sample volume can result in a smaller EPR signal; therefore, the THz EPR experiment is often performed without a resonator.[22–24] As an alternative approach, surface resonators have been studied recently.[25] The surface resonators have an advantage in securing a wide sample surface, which is not limited by the wavelength, and achieving a high concentration of the electromagnetic field in the sample region, consequently enhancing the coupling of electromagnetic waves to a sample.[26–30] In addition, the surface resonators are beneficial for the investigation of thin materials such as thin films and two-dimensional materials and have the capability to implement the access of optical and electrical stimuli for optically detected magnetic resonance (ODMR) and electrically detected magnetic resonance (EDMR).

In this work, we report the development of a double split-ring resonator (DSRR) operating at a frequency of 115 GHz. The DSRR consists of a pair of metallic loops with slits positioned at opposite sides. Split-ring resonators are widely studied in the microwave and THz wave regimes. In particular, metamaterials[31–33] based on split-ring resonators, which utilize the tunability of electromagnetic wave profiles to control the propagation profile of electromagnetic waves, have been investigated extensively.[34,35] In the DSRR device, the electric flux of the 115 GHz waves induces currents. While the slits prevent currents from flowing around the rings, capacitive current between the rings becomes considerable, consequently enhancing the induced magnetic flux inside the rings.[32] In the present study, we first discuss the design and the expected performance of the 115 GHz DSRR. Then, we describe the fabrication of the DSRR devices using photolithography and chemical etching techniques. We also describe a method to characterize individual DSRR devices and discuss the results of the characterization. The characterization shows that the variation of the resonant frequencies is from 111.50 to 114.12 GHz while the designed frequency is 113.26 GHz, corresponding to a deviation of <1.6%. The present development paves the way for the improvement of the coupling between THz waves and samples in high-frequency EPR, ODMR, and EDMR experiments.

II. DESIGN OF 115 GHz DOUBLE SPLIT-RING RESONATOR

First, the design of the 115 GHz DSRR device is discussed. The design of the DSRR is shown in Fig. 1(a). The DSRR, fabricated on the surface of a substrate, consists of a pair of rings, and the center points of both rings are the same. Each ring has gaps, and those gaps are located on opposite sides. In the present DSRR design, the smaller ring has an inner diameter of $D^{I} = 50\,\mu$m, while the larger ring has an inner diameter of $D^{O} = 190\,\mu$m, and both rings are $30\,\mu$m wide (W^{I}_{turn} and W^{O}_{turn}). Therefore, the diameters at the center of the rings are 65 and $205\,\mu$m for the inner and outer rings, respectively. In addition, both rings have a $30\,\mu$m gap (W^{I}_{gap} and W^{O}_{gap}) as shown in Fig. 1(a). Figure 1(b) shows the reflection (S_{11}) and transmission (S_{21}) calculated using CST Studio (Dassault Systems). In the calculation, we considered the rings made out of copper and the substrate made of a borosilicate glass [relative dielectric constant value ($\varepsilon_{substrate}$) of 6.4].[36] The simulation model also used the ring thickness of $10\,\mu$m, the substrate length of $500\,\mu$m, the substrate width of $500\,\mu$m, and the substrate height of $150\,\mu$m. To obtain the resonance frequency and the Q-factor, we also performed a least-square fit to the transmission data using the Fano resonance function, modeling an asymmetric resonance line shape. As can be seen, the fit and simulation agree well. We obtained that the resonance frequency (f_{res}) is 113.26 ± 0.03 GHz, and the calculated quality factor (Q-factor) is 34 ± 1.

Furthermore, a profile of the magnetic field components of the electromagnetic waves at the resonant frequency is calculated using CST Studio. The result is summarized in Fig. 2. Figure 2(a) shows a contour plot of the real part of the magnetic fields around the DSRR device. As can be seen, a high intensity of the magnetic field is displayed between the inner and outer rings. Figures 2(b)–2(d) show the z-component of the magnetic field. Figure 2(b) shows the z-component of the magnetic field amplitude as a function of the z-position (perpendicular to the DSRR plane), where $x = y = 0$.

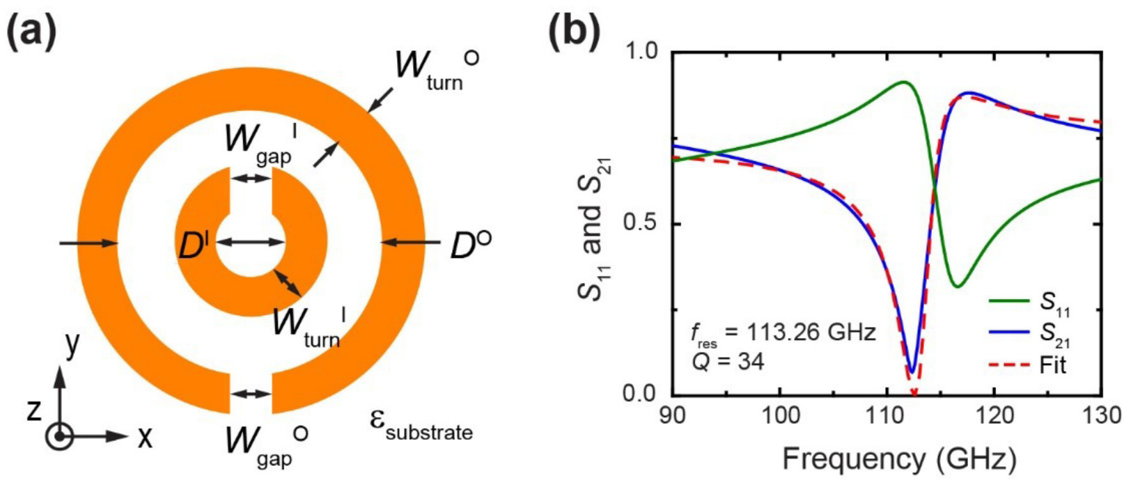

FIG. 1. A design of the 115 GHz DSRR. (a) The dimensions of the DSRR device. The substrate with a dielectric constant of $\varepsilon_{substrate}$ is positioned behind the DSRR device. (b) The calculated S_{11} and S_{21} signals based on the DSRR design is shown in Fig. 1(a). The resonance (f_{res}) is shown at 113.26 ± 0.03 GHz. The quality factor is $Q = 34 \pm 1$. The Fano resonance function, A $[q\,(\Delta f/2) + (f - f_{res})]^2/[(\Delta f/2)^2 + (f - f_{res})^2]$, was used for the fit. $f_{res} = 113.26 \pm 0.03$ GHz, $\Delta f = 3.34 \pm 0.05$ GHz, $q = 0.417 \pm 0.008$, and $A = 0.742 \pm 0.002$. The errors represent the 95% confidence interval. Using the results, we obtained $Q = f_{res}/\Delta f = 34 \pm 1$, where the error was calculated using error propagation. In the simulation, the DSRR device is placed on the front surface of the substrate. The microwave was input from the back surface of the substrate. The electric field polarization of the input was set along the x axis, which is parallel to the W^{O}_{gap} and W^{I}_{gap} directions.

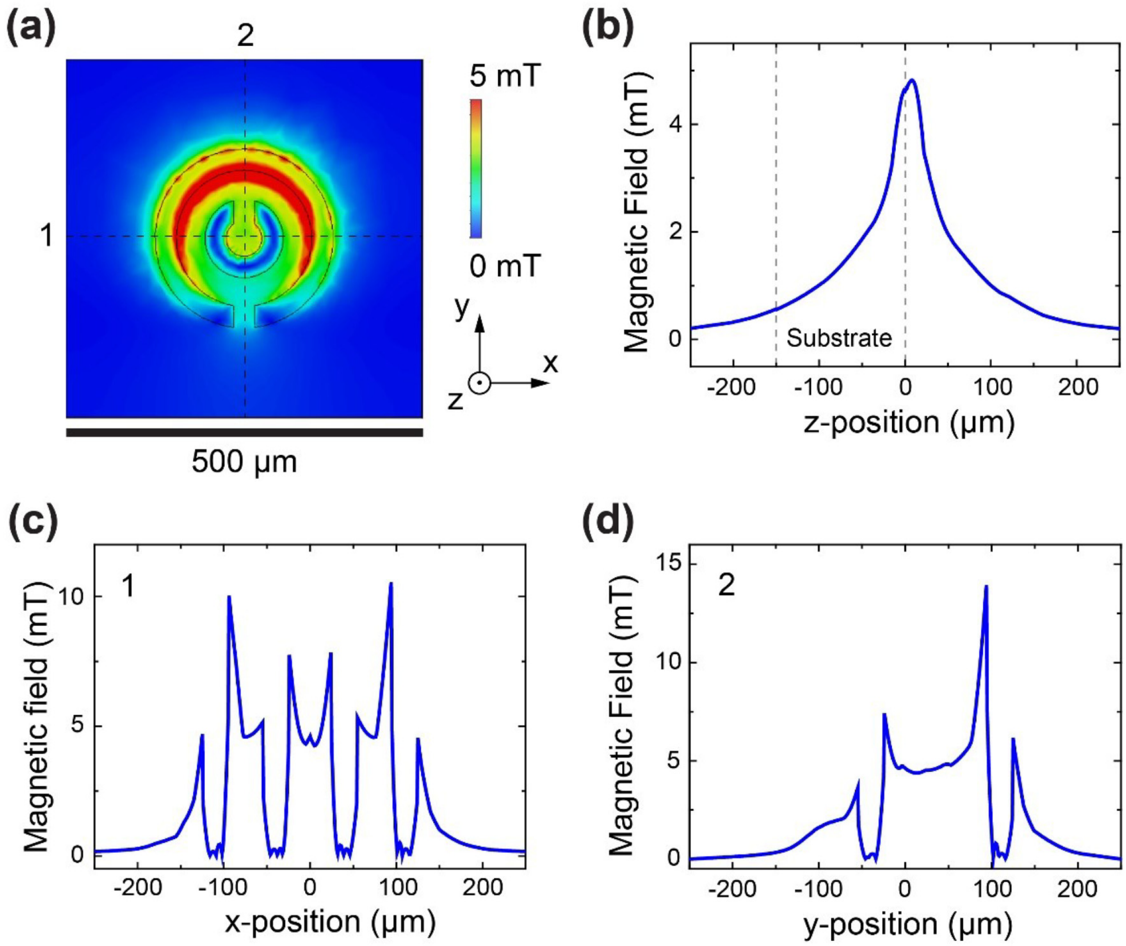

FIG. 2. The results of induced magnetic fields in the DSRR device. In the simulation, the input electromagnetic waves are with a frequency of 113.26 GHz. The input power was set at 1 W. (a) Contour plot of the real part of the induced magnetic field at z = 0. (b) Z-component of the magnetic field amplitude $\left(=\sqrt{Re^2+Im^2}\right)$, where *Re* and *Im* represent the real and imaginary parts, respectively, calculated as a function of position in the x-direction. $y = z = 0$. (c) Magnetic field strength measured as a function of position in the y-direction. $x = z = 0$. (d) Magnetic field strength measured as a function of position in the z-direction. $x = y = 0$.

As shown, the maximum value is observed at $z = 0$, corresponding to the interface between the DSRR device and the substrate. Moreover, the magnetic field profiles along the x- and y-axes are shown in Figs. 2(c) and 2(d), respectively. The profiles show that the magnetic field amplitude is high near the inner edge of the outer ring. The simulation also shows that the strength of the induced magnetic field can exceed 10 mT with the incident microwave power of 1 W, corresponding to a Rabi oscillation frequency of approximately 280 MHz.

III. FABRICATION

The DSRR devices were fabricated using a wet-etch photolithography process. The fabrication recipe is shown in Fig. 3. First, the surface of a glass cover slip is cleaned by a plasma etching process for 1 min. The cover slip is then coated with titanium with a thickness of 5 nm for adhesion, and then a copper layer with a thickness of ∼1 μm using a sputtering technique. Positive tone photoresist (AZ1512) is then coated on the copper surface using a spin coating with a revolution speed of 2150 rpm and a duration of 1 min. After the spin coating, the substrate with the photoresist is prebaked at 90 °C for 90 s to harden the photoresist [see Fig. 3(a)]. Next, as shown in Fig. 3(b), the cover slip is positioned under the photomask using an MJB3 mask aligner (Karl Suss) and is exposed to a UV light source. The UV source is set at a power of 5.3 mW/cm^2 for an exposure time of 30 s in the present procedure. After the exposure, a developer solution consisting of a 3:8 mixture of Microposit 351 developer and water is applied to the substrate to remove unhardened photoresist. Then, the exposed copper is removed by chemical etching with ferric chloride solution, and the remaining exposed titanium layer is removed using titanium etchant TFTN (Transene) [Fig. 3(c)]. Finally, as shown in Fig. 3(d),

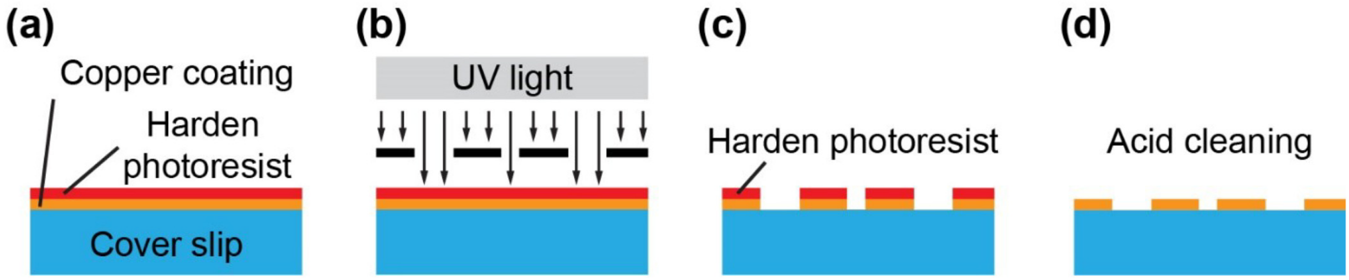

FIG. 3. Overview of the DSRR fabrication procedure. (a) Substrate coated by copper and photoresist. (b) UV light exposure over the masked substrate. (c) Development and the chemical etching process. (d) Acid cleaning process.

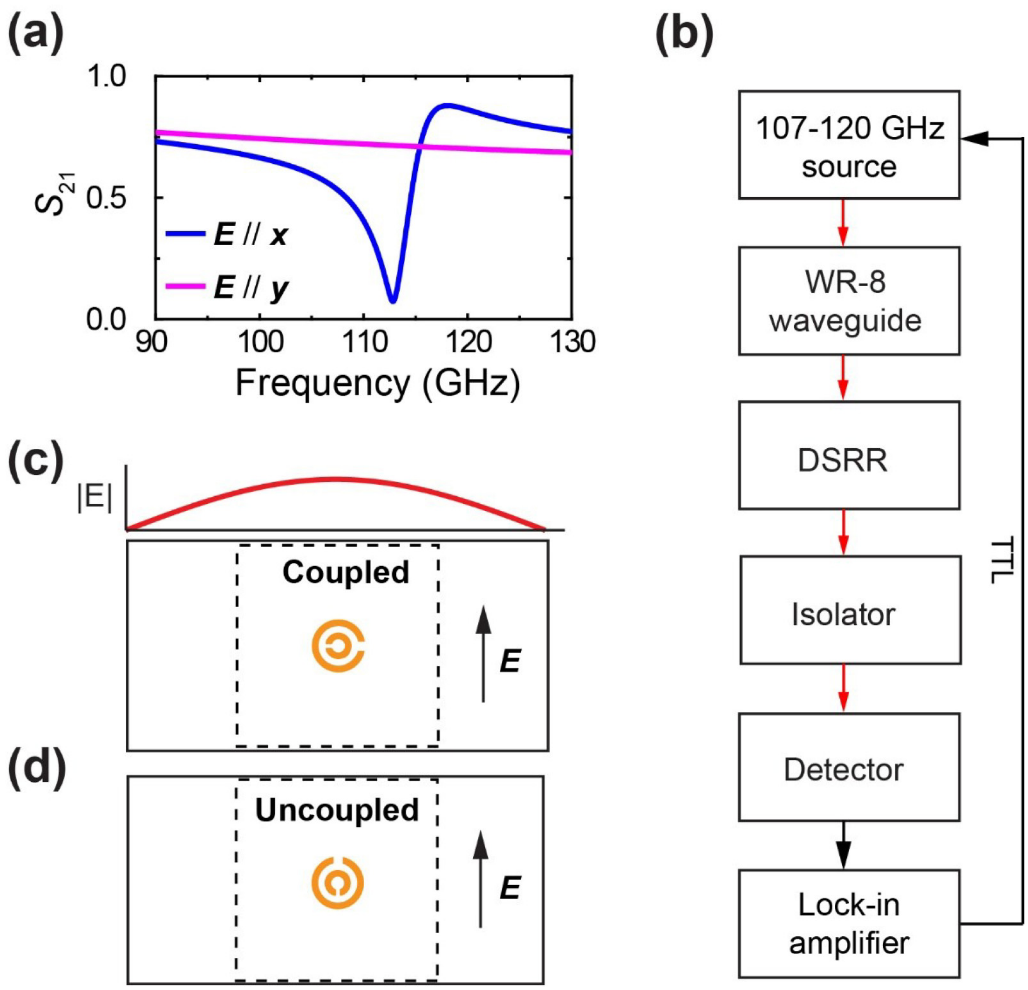

FIG. 4. Characterization of a single 115 GHz DSRR. (a) S_{21} simulation results for the coupled and uncoupled configurations performed by CST Studio. The electric field polarization was set to be parallel and perpendicular to the *x* axis (see Fig. 1 for the directions of the *x* axis). (b) A schematic of the experimental setup. (c) DSRR coupled to electromagnetic waves in the WR-8 waveguide. The dimensions of the WR8 waveguide are $1.016 \times 2.032\,\text{mm}^2$. The inset shows the intensity of the y-component of the electric field. The resonator is positioned at the center of the WR-8 waveguide. The dashed line represents the substrate. (d) DSRR uncoupled to electromagnetic waves in the WR-8 waveguide.

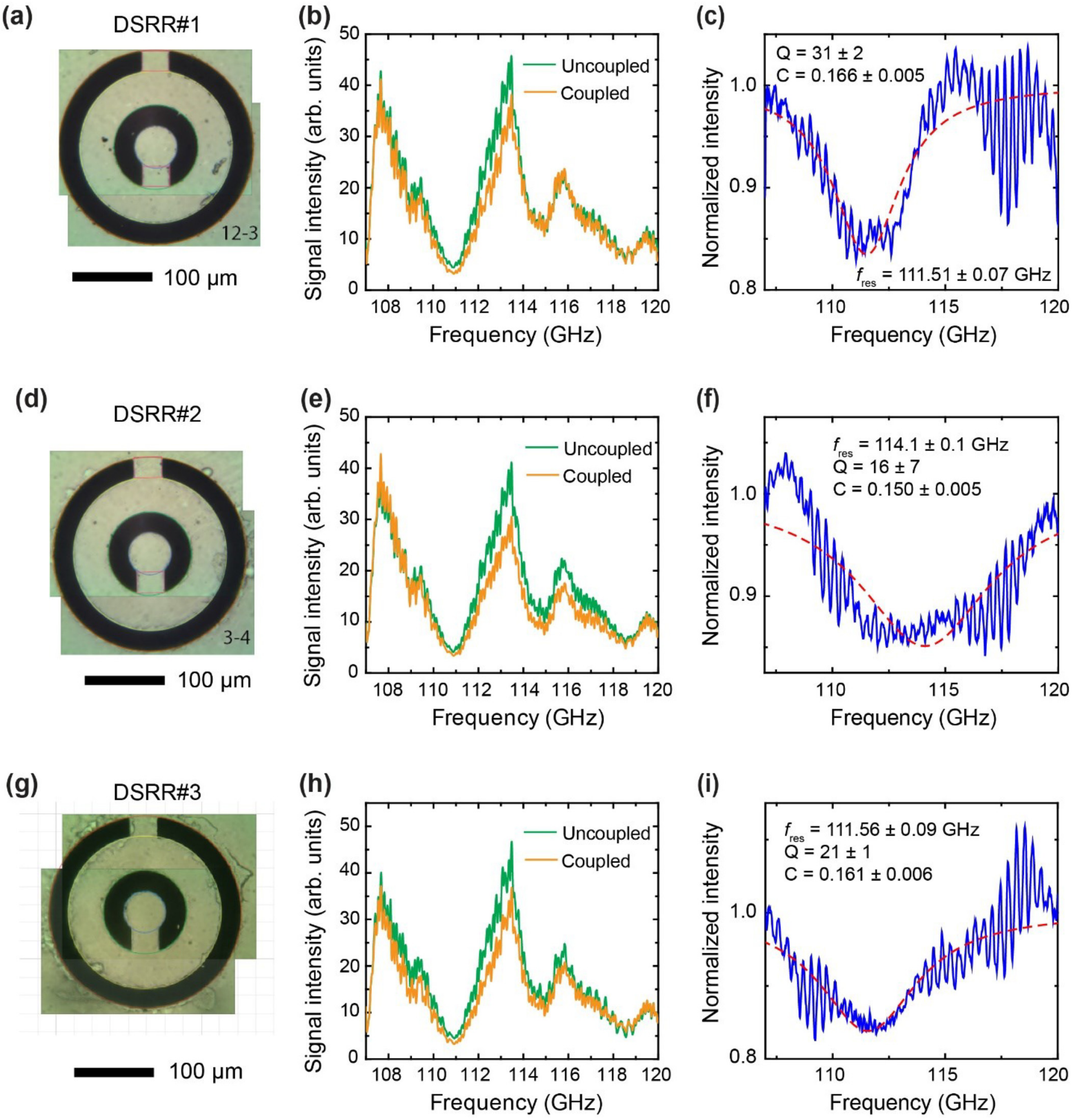

FIG. 5. Characterization of DSRR devices. (a)–(c) DSSR#1. (a) Microscope image with scale bars. (b) Microwave transmission powers with uncoupled (green) and coupled (orange) configurations, respectively. (c) Normalized intensity [$\sqrt{(I_c/I_u)}$] of the transmission. By fitting to the Lorentzian function, f_{res} = 111.51 ± 0.07 GHz, and the *Q*-factor, *Q* = 31 ± 2, were determined. (d)–(f) DSRR#2. (d) Microscope image. (e) Transmission powers with coupled and uncoupled configurations, I_c and I_u, respectively. (f) Normalized intensity [$\sqrt{(I_c/I_u)}$] as a function of microwave frequency. (g)-(i) DSRR#3. (g) Microscope image. (h) Transmission powers with coupled and uncoupled configurations, I_c and I_u, respectively. (i) Normalized intensity [$\sqrt{(I_c/I_u)}$] as a function of microwave frequency.

the remaining photoresist is removed using acetone. The physical dimensions of the fabricated DSRR devices were measured using a profilometer and by analyzing optical microscope images. Since multiple resonators were fabricated simultaneously, we checked the dimensions of the DSRR devices at various locations from the center to the outside of the substrate.

IV. CHARACTERIZATION

The resonances of the DSRR devices were characterized by measuring the absorption of electromagnetic waves. In the present case, we obtain the absorption of DSRR by measuring the changes in transmitted power with and without the coupling to the DSRR device using a rectangular waveguide. In principle, as we described previously, electromagnetic waves couple to the DSRR device when the electric field polarization of the electromagnetic waves is parallel to the direction of the gaps. Therefore, it is possible to achieve the maximum coupling by placing the gap direction [$\boldsymbol{E} /\!/ \boldsymbol{x}$ in Fig. 1(a)] parallel to the electric field and the minimum coupling by placing it perpendicular to the electric field. Figure 4(a) shows the simulated transmission (S_{21}) for the coupled ($\boldsymbol{E} /\!/ \boldsymbol{x}$) and uncoupled ($\boldsymbol{E} /\!/ \boldsymbol{y}$) configurations. As shown, the resonance is seen only in the coupled configuration. In the present case, we employ the TE_{10} mode of a WR8 rectangular waveguide to form the electric field component along the width direction (the shorter side of the rectangle) and control the coupled and uncoupled configurations by rotating the DSRR device in the waveguide. Figure 4(b) illustrates the schematic for the characterization experiment. The setup consists of a microwave source (VDI), WR-8 waveguide, DSRR, isolator (Eravant), and detector (Pacific Millimeter). The frequency of the microwave source is adjustable from 107 to 120 GHz. The frequency range of the WR8 waveguide is 90–140 GHz. The isolator is used to reduce the standing wave in the system. In the transmission measurement, the amplitude of the microwave source is modulated using a p–i–n switch, and the transmitted signal is detected using the detector and a lock-in amplifier (Stanford Research Systems). Figures 4(c) and 4(d) show the configurations of the DSRR device with and without coupling, respectively. The DSRR device is placed in the center of the waveguide to maximize the microwave intensity, as shown in Fig. 4(c). In the experiment, a substrate with dimensions of approximately $1 \times 1\,\text{mm}^2$ and a DSRR device centered on the substrate is prepared using a dicing saw, and the DSRR device is fixed inside the waveguide using a small amount of silicone vacuum grease or a small piece of thin double-sided tape on the side surface of the substrate.

Figure 5 shows the dimensions and absorption characterization of DSRR devices. The dimensions were measured from the microscope image. For example, from the analysis of Fig. 5(a), we obtained $D^{\mathrm{I}} = 54 \pm 1\,\mu$m, $D^{\mathrm{O}} = 192 \pm 1\,\mu$m, $W^{\mathrm{I}}_{\mathrm{gap}} = 35 \pm 1\,\mu$m, $W^{\mathrm{O}}_{\mathrm{gap}} = 36 \pm 1\,\mu$m, $W^{\mathrm{I}}_{\mathrm{turn}} = 24 \pm 1\,\mu$m, and $W^{\mathrm{O}}_{\mathrm{turn}} = 23 \pm 1\,\mu$m for DSRR#1. Figure 5(b) shows the transmission power of the DSRR device with the coupled (I_c) and uncoupled (I_u) configurations. Peaks and dips shown in the transmission powers are mainly due to the standing waves. As can be seen, the transmission power of I_c is smaller than that of I_u in the range of 108 and 114 GHz, while I_c and I_u are similar above 114 GHz. The result indicates that the difference is due to the THz absorption by DSRR. Then, the normalized transmission intensity is obtained by calculating $\sqrt{(I_c/I_u)}$ to remove the standing wave contributions. Note that the square-root was imposed to convert the power transmission coefficient to the transmission coefficient and to compare with the simulated S_{21}, as shown in Fig. 1. By fitting the normalized intensity with the Lorentzian function, we obtained the resonance frequency (f_{res}), the Q-factor (Q), and the contrast of the resonance (C) to be 111.51 ± 0.07 GHz, 31 ± 2, and 0.166 ± 0.005 for DSRR#1, respectively [Fig. 5(c)]. In the fit, the background of the normalized intensity was set to be 1. Moreover, we fabricated and characterized two more DSRR devices with the same method described previously, and their results are shown in Figs. 5(d)–5(i).

Moreover, the resonance frequencies, Q-factors, and the dimensions are summarized in Table I. As can be seen, $\mathrm{D^I}$ and $\mathrm{D^O}$ are larger than the designed values while $\mathrm{W^I_{turn}}$ and $\mathrm{W^O_{turn}}$ are smaller. We also obtained that the center diameters of the fabricated inner rings are 66 ± 1, 66 ± 1, and $66 \pm 1\,\mu$m for DSRR#1, 2, and 3, respectively (the designed value is $65\,\mu$m). Similarly, the center diameters of the fabricated outer rings are 204 ± 1, 203 ± 1, and $206 \pm 1\,\mu$m for DSRR#1, 2, and 3, respectively, while the designed value is $205\,\mu$m. Therefore, the result shows that the sizes of both rings are within the specification, but the widths of DSRR rings are slightly smaller than the designed values. This probably originates from the fabrication. As summarized, the measured resonant frequencies vary from 111.51 to 114.1 GHz. Because the simulated value is 113.26 GHz, the deviations of the resonant frequencies from the simulation are less than 1.6%. The Q-factors vary from 16 to 31 (the variation of ∼50%). Moreover, the characterization results showed that the resonance contrast is higher when the Q-factor of the DSRR is higher, and the contrast varies from 0.150 to 0.166, corresponding to a variation of ∼10%. This variation is smaller than that of the Q-factor, which implies a nontrivial contribution of radiation to the resonator Q-factor, i.e., magnetic fields induced around the DSRR.

Next, the relationships between the dimensions of the larger and smaller rings and the measured resonant frequencies and Q-factors are discussed. Figure 6 shows the resonance frequencies and Q-factors as a function of dimensions. Figures 6(a)–6(c) are the plots for the larger ring, and Figs. 6(d)–6(f) are the plots for

TABLE I. Dimensions of fabricated DSRR devices. The unit of the dimensions is in μm.

#	$\mathrm{D^I}$ (50)	$\mathrm{D^O}$ (190)	$\mathrm{W^I_{gap}}$ (30)	$\mathrm{W^O_{gap}}$ (30)	$\mathrm{W^I_{turn}}$ (30)	$\mathrm{W^O_{turn}}$ (30)	f_{res} (GHz)	Q
1	54 ± 1	192 ± 1	35 ± 1	36 ± 1	24 ± 1	23 ± 1	111.51 ± 0.07	31 ± 2
2	54 ± 1	191 ± 1	34 ± 1	34 ± 1	24 ± 1	24 ± 1	114.1 ± 0.1	16 ± 7
3	53 ± 1	194 ± 1	36 ± 1	35 ± 1	25 ± 1	24 ± 1	111.56 ± 0.09	21 ± 1

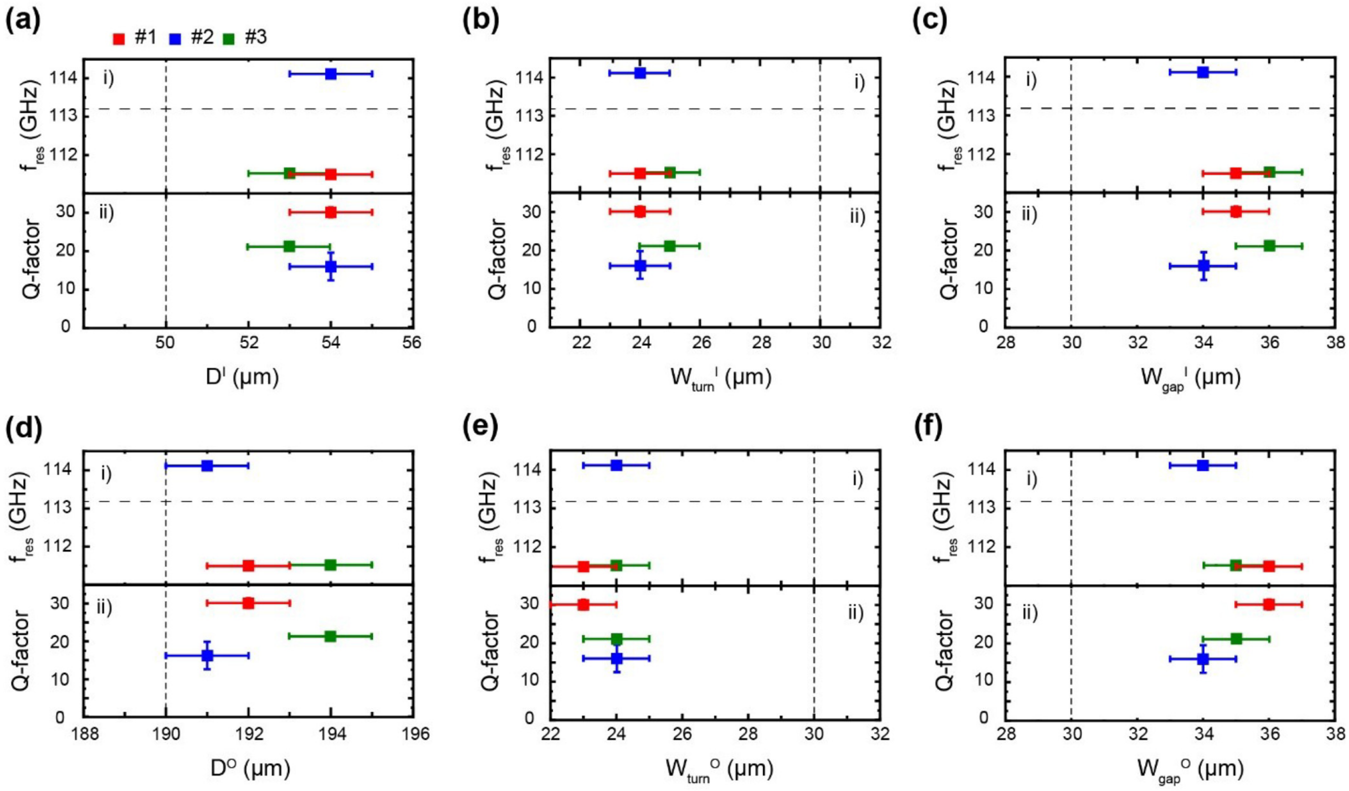

FIG. 6. Resonant frequencies and Q-factors of resonators vs their dimensions. The resonant frequencies f_{res} are shown in (i). The Q-factors are shown in (ii). (a) f_{res} and Q-factor vs D^I. (b) f_{res} and Q-factor vs W^I_{turn}. (c) f_{res} and Q-factor vs W^I_{gap}. (d) f_{res} and Q-factor vs D^O. (e) f_{res} and Q-factor vs W^O_{turn}. (f) f_{res} and Q-factor vs W^O_{gap}.

the smaller ring. As can be seen in Figs. 6(a) and 6(b), there is no pronounced correlation between the resonant frequencies, Q-factors, D^O, and W^O_{turn}. On the other hand, although the number of data points is limited, Fig. 6(c) suggests that the resonant frequencies increase when W^O_{gap} is larger. In addition, Figs. 6(d)–6(f) show no clear correlation between the resonant frequencies, Q-factors, and the dimensions for the smaller ring. Overall, the result suggests that the resonant frequencies and Q-factors remain in the designed range with the observed small difference in the dimensions.

V. SUMMARY

In summary, we fabricated 115 GHz DSRR devices for a frequency of 115 GHz using photolithography and chemical etching techniques. We also developed a characterization method, which allows us to measure the absorption of individual DSRR devices. Our characterization shows that the deviations of resonant frequencies of the fabricated DSRR devices are less than 1.6%. The presented method can be extended to build DSRR devices for higher THz frequencies and the applications to ODMR and EDMR spectroscopy, where it is often challenging to integrate the resonator, optical, and electrical accesses together in a limited space.

ACKNOWLEDGMENTS

We thank Donghai Zhu and the USC core nanofabrication facilities for the support of the DSRR fabrication. This work was supported by the National Science Foundation (Grant Nos. CHE-2404463 and CHE-2004252 with partial co-funding from the Quantum Information Science program in the Division of Physics) and the Zumberge Foundation (ST).

AUTHOR DECLARATIONS

Conflict of Interest

The authors have no conflicts to disclose.

Author Contributions

Gem Nakamura: Data curation (equal); Formal analysis (equal); Investigation (equal); Validation (equal); Visualization (equal). **Yuhang Ren:** Data curation (equal); Formal analysis (equal); Investigation (equal); Validation (equal); Visualization (equal). **Michael Coumans:** Investigation (equal); Methodology (equal). **Laura Mugica:** Investigation (equal). **Sola M. Takahashi:** Formal analysis (equal); Methodology (equal); Software (equal); Visualization (equal). **Anton Savitsky:** Conceptualization (equal); Investigation (equal); Methodology (equal); Software (equal). **Dieter Suter:** Conceptualization (equal); Investigation (equal); Methodology (equal); Software (equal). **Susumu Takahashi:** Conceptualization (equal); Data curation (equal); Formal analysis (equal); Funding acquisition (equal); Investigation (equal); Methodology (equal); Project administration (equal); Resources (equal); Software (equal); Supervision (equal); Validation (equal); Visualization (equal); Writing – original draft (equal); Writing – review & editing (equal).

DATA AVAILABILITY

The data that support the findings of this study are available from the corresponding author upon reasonable request.

REFERENCES

[1] D. M. Mittleman, J. Appl. Phys. **122**(23), 230901 (2017).
[2] P. A. Banks, E. M. Kleist, and M. T. Ruggiero, Nat. Rev. Chem. **7**(7), 480–495 (2023).
[3] D. F. Swearer, S. Gottheim, J. G. Simmons, D. J. Phillips, M. J. Kale, M. J. McClain, P. Christopher, N. J. Halas, and H. O. Everitt, ACS Photonics **5**(8), 3097–3106 (2018).
[4] M. Lou, D. F. Swearer, S. Gottheim, D. J. Phillips, J. G. Simmons, Jr., N. J. Halas, and H. O. Everitt, Rev. Sci. Instrum. **90**(5), 053110 (2019).
[5] C. K. Michael, P. F. Taday, E. C. Bryan, J. A. Cluff, J. F. Anthony, and R. T. William, Proc. SPIE **5070** (2003).
[6] D. G. Allis and T. M. Korter, ChemPhysChem **7**(11), 2398–2408 (2006).
[7] H. Hoshina, Y. Sasaki, A. Hayashi, C. Otani, and K. Kawase, Appl. Spectrosc. **63**(1), 81–86 (2009).
[8] K. Kawase, Opt. Photon. News **15**(10), 34–39 (2004).
[9] J. H. Freed, Annu. Rev. Phys. Chem. **51**(1), 655–689 (2000).
[10] S. Takahashi, G. Ramian, M. S. Sherwin, L.-C. Brunel, and J. van Tol, Appl. Phys. Lett. **91**(17), 174102 (2007).
[11] S. Takahashi, L.-C. Brunel, D. T. Edwards, J. van Tol, G. Ramian, S. Han, and M. S. Sherwin, Nature **489**(7416), 409–413 (2012).
[12] S. Takahashi, R. Hanson, J. van Tol, M. S. Sherwin, and D. D. Awschalom, Phys. Rev. Lett. **101**(4), 047601 (2008).
[13] Z. Peng, T. Biktagirov, F. H. Cho, U. Gerstmann, and S. Takahashi, J. Chem. Phys. **150**, 134702 (2019).
[14] Y. Ren, C. Selco, D. Kawashiri, M. Coumans, B. Fortman, L. S. Bouchard, K. Holczer, and S. Takahashi, Phys. Rev. B **108**, 045421 (2023).
[15] B. Fortman, J. Pena, K. Holczer, and S. Takahashi, Appl. Phys. Lett. **116**(17), 174004 (2020).
[16] S. Takahashi, J. van Tol, C. C. Beedle, D. N. Hendrickson, L.-C. Brunel, and M. S. Sherwin, Phys. Rev. Lett. **102**(8), 087603 (2009).
[17] S. Takahashi, I. S. Tupitsyn, J. van Tol, C. C. Beedle, D. N. Hendrickson, and P. C. E. Stamp, Nature **476**(7358), 76–79 (2011).
[18] C. Abeywardana, A. M. Mowson, G. Christou, and S. Takahashi, Appl. Phys. Lett. **108**, 042401 (2016).
[19] D. T. Edwards, S. Takahashi, M. S. Sherwin, and S. Han, J. Magn. Reson. **223**, 198–206 (2012).
[20] C. P. Poole, *Electron Spin Resonance: A Comprehensive Treatise on Experimental Techniques*, 2nd ed. (Wiley, New York, 1983).
[21] S. Takahashi and S. Hill, Rev. Sci. Instrum. **76**, 023114 (2005).
[22] J. van Tol, L.-C. Brunel, and R. J. Wylde, Rev. Sci. Instrum. **76**, 074101 (2005).
[23] F. H. Cho, V. Stepanov, and S. Takahashi, Rev. Sci. Instrum. **85**, 075110 (2014).
[24] F. H. Cho, V. Stepanov, C. Abeywardana, and S. Takahashi, Methods Enzymol. **563**, 95 (2015).
[25] L. Tesi, D. Bloos, M. Hrtoň, A. Beneš, M. Hentschel, M. Kern, A. Leavesley, R. Hillenbrand, V. Křápek, T. Šikola, and J. van Slageren, Small Methods **5**(9), 2100376 (2021).
[26] R. Narkowicz, D. Suter, and I. Niemeyer, Rev. Sci. Instrum. **79**(8), 084702 (2008).
[27] R. Narkowicz, D. Suter, and R. Stonies, J. Magn. Reson. **175**(2), 275–284 (2005).
[28] A. Banholzer, R. Narkowicz, C. Hassel, R. Meckenstock, S. Stienen, O. Posth, D. Suter, M. Farle, and J. Lindner, Nanotechnology **22**(29), 295713 (2011).
[29] C. Clauss, M. Dressel, and M. Scheffler, J. Phys.: Conf. Ser. **592**(1), 012146 (2015).
[30] N. Abhyankar, A. Agrawal, P. Shrestha, R. Maier, R. D. McMichael, J. Campbell, and V. Szalai, Sci. Adv. **6**(44), eabb0620 (2020).
[31] V. G. Veselago, Sov. Phys. Usp. **10**(4), 509 (1968).
[32] J. B. Pendry, A. J. Holden, D. J. Robbins, and W. J. Stewart, IEEE Trans. Microw. Theory Tech. **47**(11), 2075–2084 (1999).
[33] J. B. Pendry, Phys. Rev. Lett. **85**(18), 3966–3969 (2000).
[34] K. Fan, A. C. Strikwerda, X. Zhang, and R. D. Averitt, Phys. Rev. B **87**(16), 161104 (2013).
[35] H. L. Phan, K. Kim, J. M. Seo, and K. I. Koo, IEEE Access **12**, 18685–18693 (2024).
[36] R. Rodriguez-Cano, N. L. Clark, J. C. Mauro, and M. T. Lanagan, AIP Adv. **14**(11), 115105 (2024).